Electronic Supplementary Material (ESI) for Journal of Materials Chemistry C.

Supporting Information: Photoluminescence coupled to electric and magnetic surface lattice resonance in periodic arrays of zirconia nanoparticles

Makoto Higashino, Shunsuke Murai,* Tien-Yang Lo, Shuhei Tomita, and Katsuhisa Tanaka

Department of Material Chemistry, Graduate School of Engineering, Kyoto University, Nishikyo-ku, Kyoto 615-8510, Japan

E-mail: murai@dipole7.kuic.kyoto-u.ac.jp

Contents

1 X-ray diffraction for the ZrN thin film before and after oxidation

The ZrO_2 thin film was prepared by heat-treating the ZrN thin film, 150 nm thick and sputter-deposited on an SiO_2 substrate, in an electric furnace at 900°C for 2 h in air, i.e., under the same condition as for the preparation of ZrO_2 nanoparticle array from ZrN nanoparticle array. The X-ray patterns show that the notable change accompanies the heat-treatment: Before the heat-treatment, all the peaks are ascribable to cubic ZrN, while all the peaks are monoclinic ZrO_2 after heat-treatment. ZrO_2 has several crystalline phases and monoclinic phase is the most stable at room temperature.

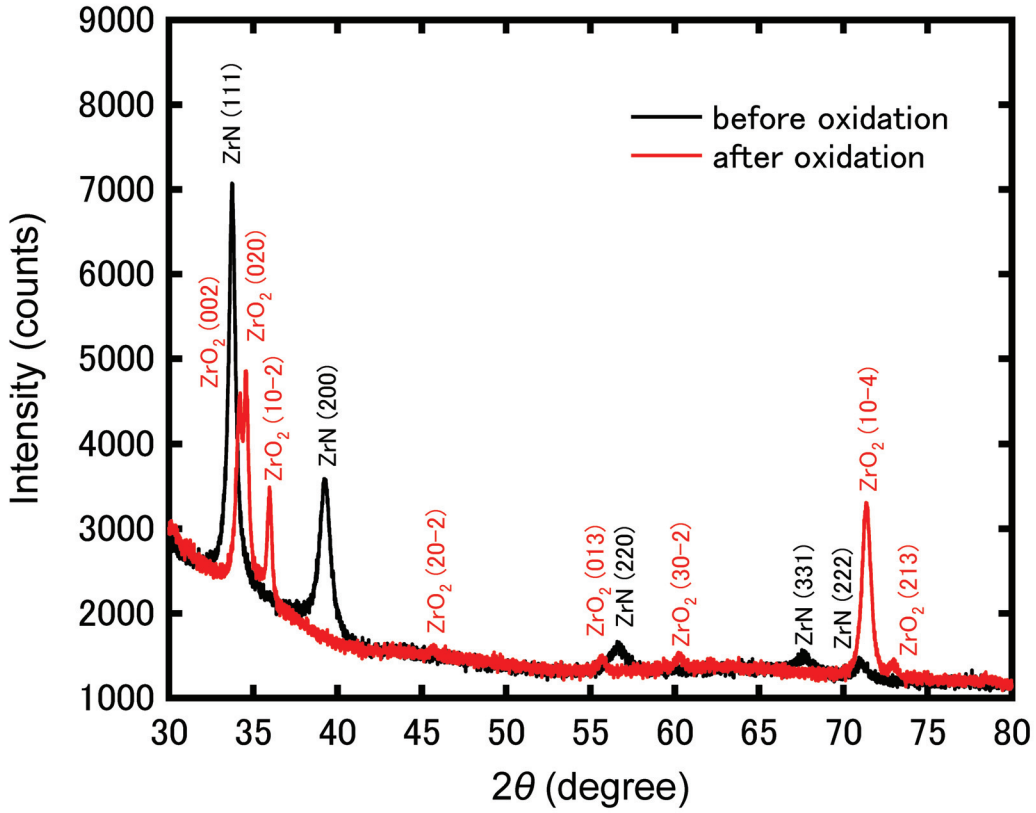

Figure S 1: X-ray diffraction patterns of the ZrN thin film on SiO_2 glass substrate: (black) before oxidation, (red) after oxidation. The assignments of the peaks from cubic ZrN and monoclinic ZrO_2 are found on top of the peaks.

2 SEM image of the ZrN nanoparticle array before oxidation

The ZrN nanoparticle hexagonal array with a=410 nm consists of nanoparticles with diameter d= 196 nm.

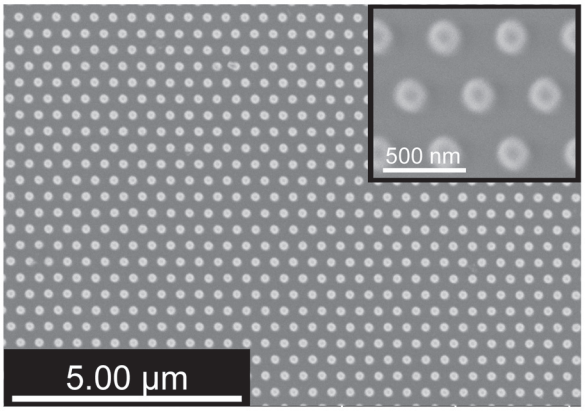

Figure S 2: Top-view SEM image of the ZrN nanoparticle array (a= 410 nm) before oxidation.

3 Extinction for the hexagonal ZrO_2 arrays with varied periodicity

Extinction spectra as a function of θ_{in} are summarized in Figs. S3 and S4. All the spectra were measured with the index-matched condition using matching oil and the upperstrate, and θ_{in} was varied in the z-x plane. The extinction for TE-polarization (Fig. S3) shows three dispersive lines along the dashed lines describing the Rayleigh anomaly. Among them, ($\pm$1,0) and (0,$\pm$1) orders, which mainly couples to electric dipoles oscillating in y-direction (p_y), are stronger than ($\pm$1,$\mp$1) orders which couples to magnetic dipoles in x-direction (m_x). The features redshift with the increase of the lattice constant a. For TM-polarization (Fig. S4), the origins of the SLRs flip, i.e, the ($\pm$1,0) and (0,$\pm$1) orders are originated mainly from magnetic dipoles (m_y), and ($\pm$1,$\mp$1) orders are from electric dipoles (p_x). The extinction due to the electric dipoles is stronger.

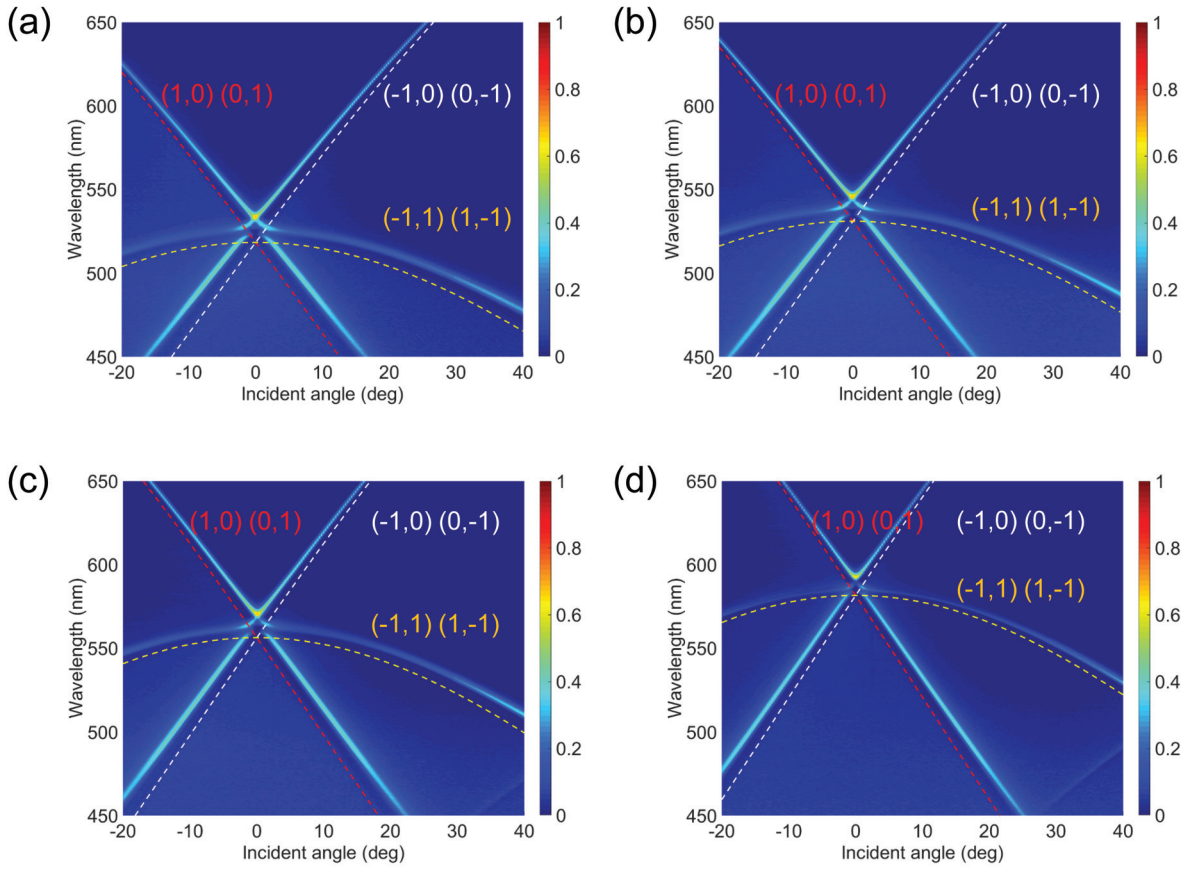

Figure S 3: Extinction of the hexagonal arrays of ZrO_2 nanoparticle with different periodicity a= (a) 410, (b) 420, (c) 440, and (d) 460 nm for TE polarization. The dashed lines denote the diffraction orders.

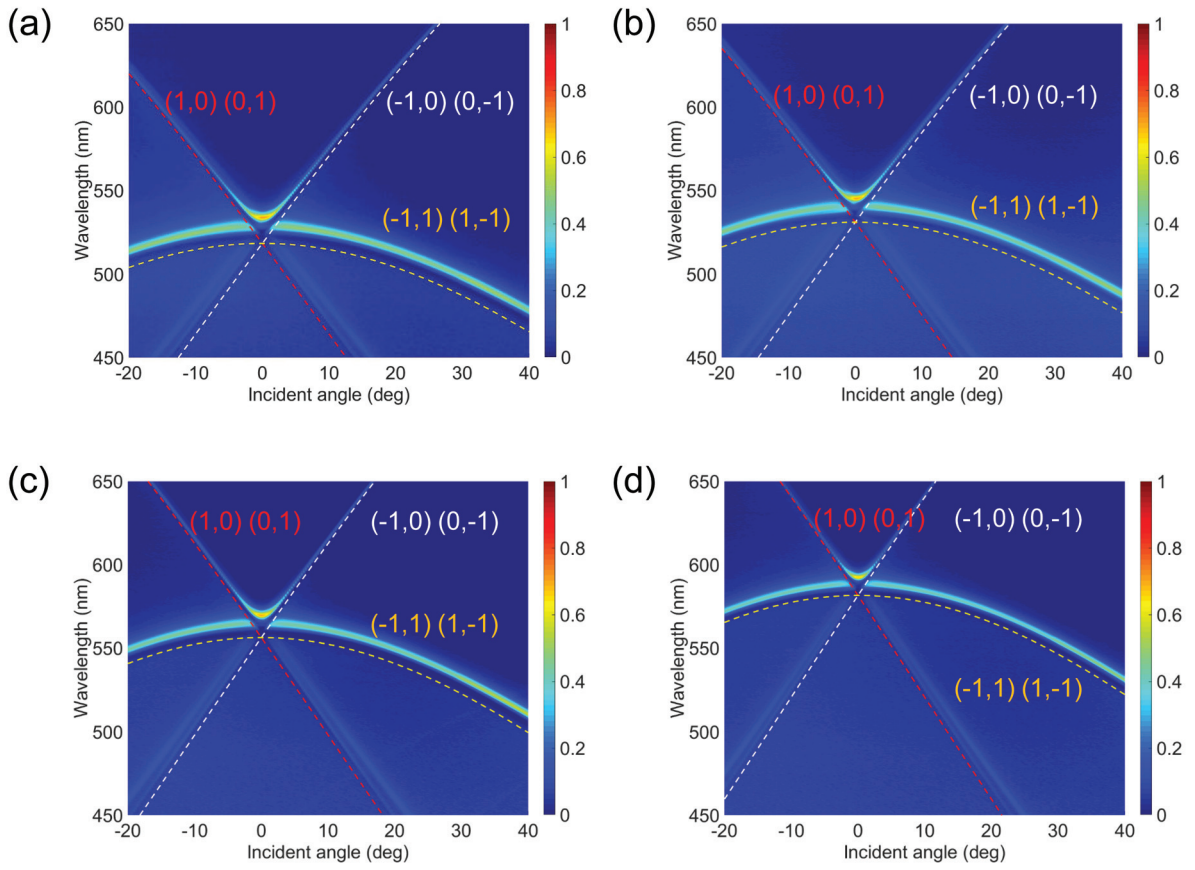

Figure S 4: Extinction of the hexagonal arrays of ZrO_2 nanoparticle with different periodicity a= (a) 410, (b) 420, (c) 440, and (d) 460 nm for TM polarization. The dashed lines denote the diffraction orders.

4 PL decays of coumarin 521T on the ZrO_2 nanoparticle hexagonal array with varied detection wavelength

The PL decays of the PMMA layer containing coumarin 521T on the ZrO_2 arrays with the detected wavelengths corresponding to the magnetic (λ= 522 nm) and electric (λ= 532 nm) SLR (see Fig. 5(b) in the main manuscript) are summarized in Figs. S5(a) and (b), respectively. At each wavelength, the decay curve is similar to that of the reference layer on the flat substrate. τ_a increases with the increase of the detection wavelength, in accordance with the decrease in the refractive index surrounding the emitter, which reduces the density of optical states and decreases the radiative decay rate (see Fig. S5(c) for comparison).

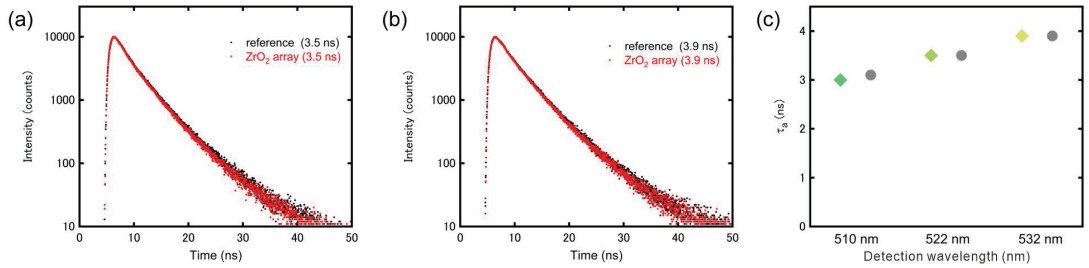

Figure S 5: PL decay curves of the PMMA layer containing coumarin 521T on the ZrO_2 hexagonal arrays with the detection wavelength corresponding to (a) magnetic (λ= 522 nm) and (b) electric (λ= 532 nm) SLR, together with the reference layer on the flat substrate. The excitation wavelength is 470 nm. The averaged PL lifetimes τ_a extracted from the experimental data are shown in the legend. (c) Comparison of τ_a at each detection wavelength. Diamonds and circles denote τ_a of the emitter layer on the array and on the flat substrate, respectively.

5 Emission from $Eu(hfa)_3(TPPO)_2$ layer on the hexagonal arrays of ZrO_2 nanoparticles

$Eu(hfa)_3(TPPO)_2$ shows four main emission lines ascribable to Eu^{3+} $^5D_0$–$^7F_1$, –$^7F_2$, –$^7F_3$ and –$^7F_4$ transitions. Since $^5D_0$–$^7F_3$ and $^5D_0$–$^7F_4$ transitions are relatively weaker compared to the others, the signals are less clear in the PL enhancement map in Fig. 6 in the main text. The zoom up views around the transitions, in Fig. S6, show a clear enhancement of these peaks.

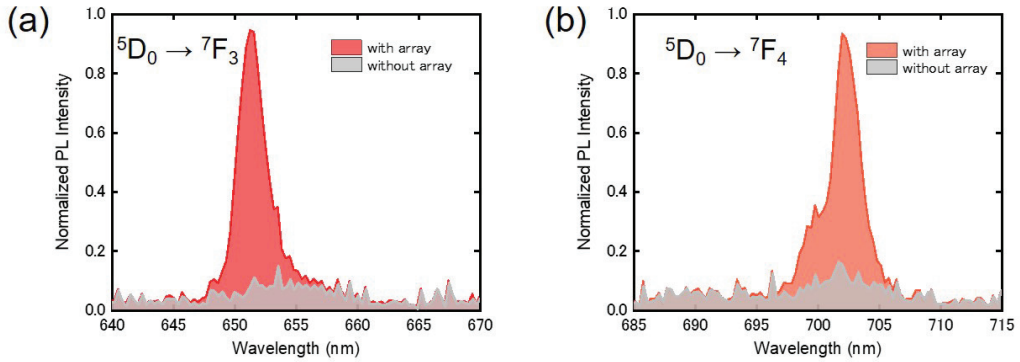

Figure S 6: PL emission of the PMMA layer containing $Eu(hfa)_3(TPPO)_2$ on the hexagonal array of ZrO_2 nanoparticle: (a) around the $^5D_0$–$^7F_3$ transition at $\theta_{em} = 12$ °, (b) around the $^5D_0$–$^7F_4$ transition at $\theta_{em} = 22$ °. PL from the reference layer on the flat substrate is also plotted as the gray area.

6 PL decays of $Eu(hfa)_3(TPPO)_2$ layer on the hexagonal arrays of ZrO_2 nanoparticles with varied periodicity

The PL decays of the PMMA layer containing $Eu(hfa)_3(TPPO)_2$ on the ZrO_2 arrays with varied periodicity are summarized in Fig. S7. All the four samples with varied periodicity show the decay curves similar to that of the reference layer on the flat substrate.

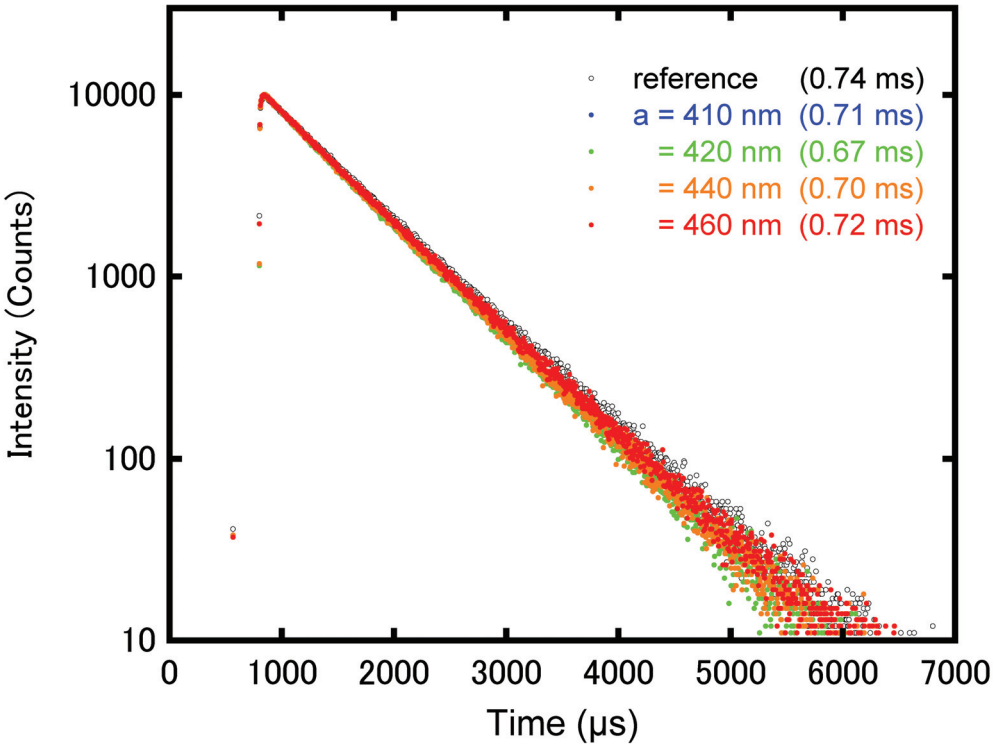

Figure S 7: PL decay curves of the PMMA layer containing $Eu(hfa)_3(TPPO)_2$ on the ZrO_2 hexagonal arrays with varied periodicity, together with the reference layer on the flat substrate. The excitation and detection wavelengths are 340 and 615 nm, respectively. The averaged PL lifetimes extracted from the experimental data are shown in the legend.

7 Structures of the ZrO_2 and TiO_2 nanoparticle square arrays

We fabricated the ZrO_2 and TiO_2 nanoparticle arrays with identical design using the same nanoimprint mold. The SEM images (Figs. S8(a) and 8(c)) show the square lattice with a= 350 nm with nanoparticle diameter of 200 and 220 nm for ZrO_2 and TiO_2 nanoparticles, respectively. The size of nanoparticle is further explored by AFM (Figs. S8(b) and 8(d)). Both arrays consist of dome-shaped nanoparticles with the height of $\sim$ 300 (ZrO_2) and 200 (TiO_2) nm.

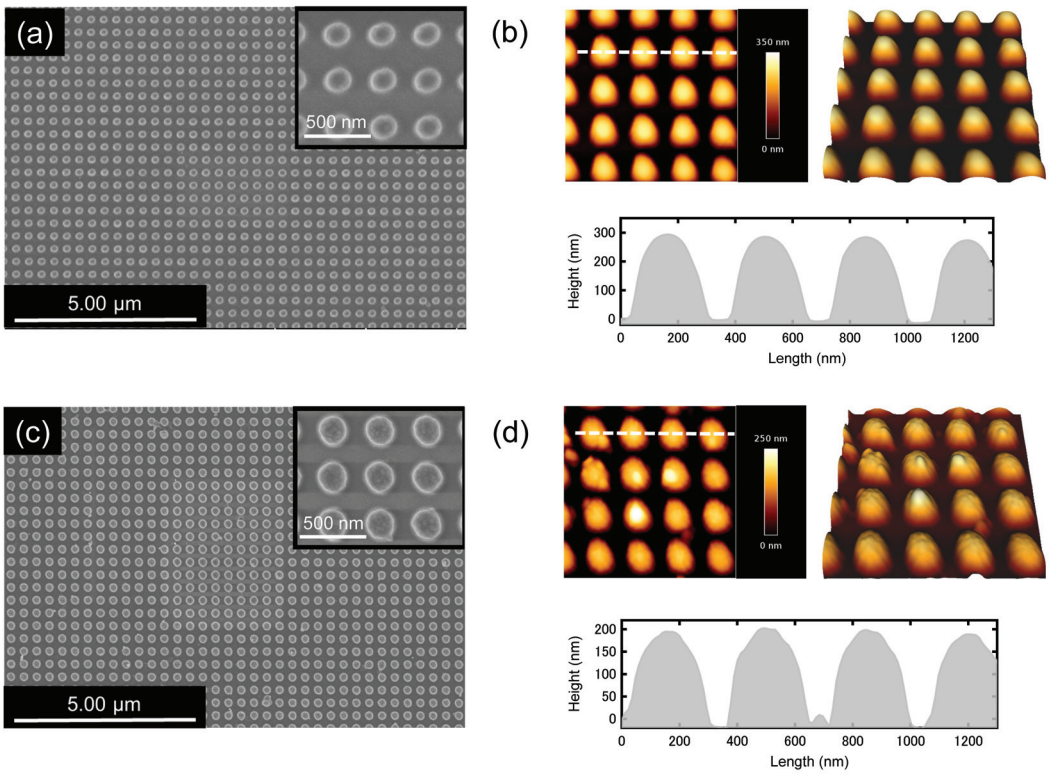

Figure S 8: (a,c) SEM images of (a) ZrO_2 and (c) TiO_2 nanoparticle square arrays. (b, d) AFM images of (b) ZrO_2 and (d) TiO_2 nanoparticle square arrays.

8 Extinction of ZrO_2 and TiO_2 nanoparticle square arrays as a function of θ_{in}

The extinction of ZrO_2 and TiO_2 nanoparticle arrays as a function of θ_{in} are summarized in Fig. S9. The measurement was conducted under homogeneous refractive index condition with matching oil. Also shown in the figure as the dashed line is Rayleigh anomaly. For square lattices, reciprocal unit vectors $\boldsymbol{b_1}$ and $\boldsymbol{b_2}$ are expressed by[1]

$$\begin{aligned} \boldsymbol{b_1} &= (2\pi/a)\hat{x} \\ \boldsymbol{b_2} &= (2\pi/a)\hat{y} \end{aligned} \tag{1}$$

and Rayleigh anomaly is given for incident light along the x-direction by

$$|\boldsymbol{k_0}|^2 = \left|\boldsymbol{k}_{||}\right|^2 + m_1^2(\frac{2\pi}{a})^2 + m_2^2(\frac{2\pi}{a})^2 + 2\left|k_{||}\right|m_1(\frac{2\pi}{a}), \tag{2}$$

where m_1 and m_2 are the diffraction orders along $\boldsymbol{b_1}$ and $\boldsymbol{b_2}$, respectively. For TE polarization in Figs. S9(a) and 9(c), SLR along (±1,0), i.e., electric SLR that couples electric dipoles along y-direction (p_{y}) is stronger. SLR along (0, ±1) splits into magnetic dipoles along x (m_{x}) and z (m_{z})-directions.[2] Under TM polarization (Figs. S9(b) and 9(d)), electric SLRs are excited along (0, ±1), being split into (p_{x}) and (p_{z}).

The SLRs sustained in the TiO_2 array are broader and redshifted with respect to those in the ZrO_2 nanoparticle array. This indicates stronger interaction between the localized Mie resonance at each nanoparticle via diffraction.[3] The localized resonance can be seen at the blue spectral region ($\lambda < 500$ nm) in Fig. S9: A broad extinction appears around λ= 450 nm for the TiO_2 nanoparticle array, while the array is transparent in the same spectral region for the ZrO_2 nanoparticle array.

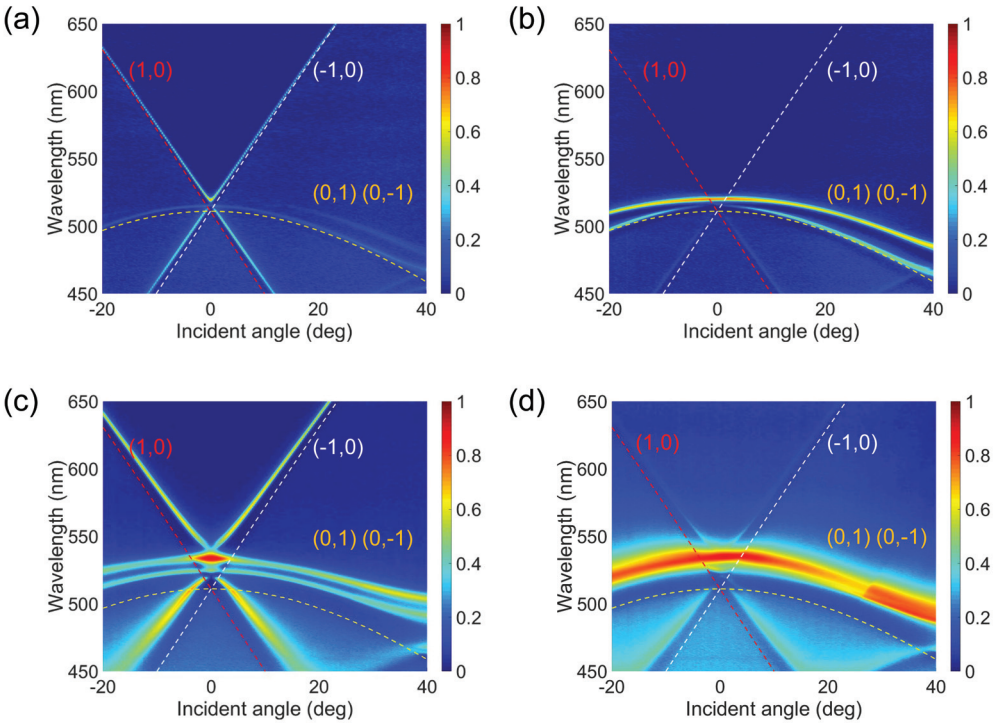

Figure S 9: Extinction of (a,b) ZrO_2 and (c,d) TiO_2 nanoparticle square arrays as a function of θ_{in}. The white dashed lines denote the diffraction orders. (a,c) TE-polarized light; (b,d) TM-polarized light.

9 PL enhancement of ZrO_2 and TiO_2 nanoparticle square arrays as a function of θ_{em}

The PL enhancement of ZrO_2 and TiO_2 nanoparticle arrays was measured as a function of θ_{em} (see Fig. S10). The measurement was conducted with a PMMA layer containing coumarin 521T (Figs. S10(a) and 10(b)) and $Eu(hfa)_3(TPPO)_2$ (Figs. S10(c) and 10(d)) for the excitation with visible (λ= 445 nm) and UV (λ= 325 nm), respectively. Angular profiles of PL enhancement follow those of the extinction: The spectra are broader for the TiO_2 nanoparticle array and redshift with respect to the ZrO_2 nanoparticle array.

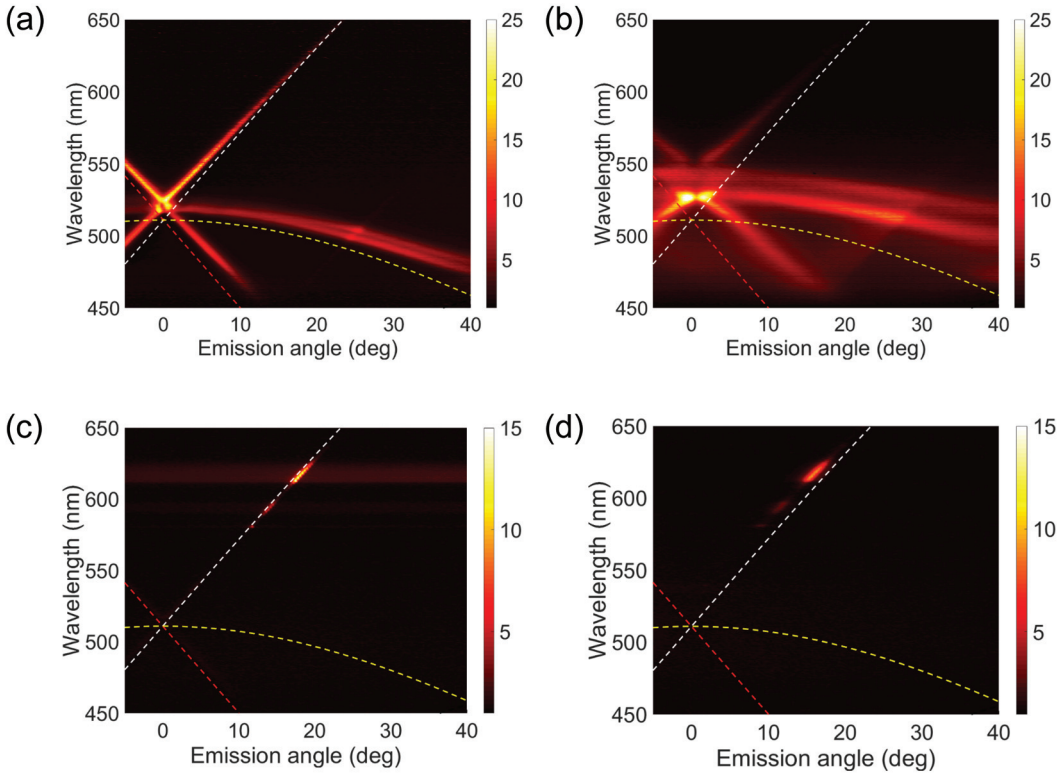

Figure S 10: PL enhancement (TE component) of (a,c) ZrO_2 and (b,d) TiO_2 nanoparticle square arrays as a function of θ_{em}. The PL enhancement is defined as the emission intensity of the emitter layer on the array normalized to that of the similar emitter layer on the flat substrate without the array. The white dashed lines denote the diffraction orders. The emitter layer is a PMMA layer containing (a,b) coumarin 521T excited with λ= 445 nm and (c,d) $Eu(hfa)_3(TPPO)_2$ excited with λ= 325 nm.

10 Simulation of optical heating

The temperature rise of the samples upon laser irradiation was numerically simulated and solved under steady-state conditions by COMSOL Multiphysics heat transfer module. We modelled the TiO_2/ZrO_2 nanoparticles embedded in the PMMA layer containing $Eu(hfa)_3(TPPO)_2$ as the thermally effective medium with a volume-weighted average thermal properties. See Table 1 for the thermal properties of each component. The effective medium (thickness = 280 nm) was placed on the SiO_2 substrate and a λ= 325 nm Gaussian beam with the spot radius of 1 mm was illuminated. We assumed that the photon energy absorbed by the material will totally be converted into heat and the effect of the convectional and radiative heat flux can be ignored. Figure S11 plots the calculated increase of the surface temperature (ΔT) at the focus point as a function of laser power density (irradiance). Temperature increases linearly with the increment of irradiance. The slope is larger for the TiO_2 sample, while that for the ZrO_2 sample is negligibly small. This difference largely comes from the difference in absorption at λ = 325 nm (see Table 2 for the input absorptance values). Under the experimental irradiance of ∼6300 W/m^2, ΔT is only 1.5 K for TiO_2, but this value can be considerably large under high power excitation.

Table 1: Material properties used for the optical heating simulation. κ, C_p, and ρ are the thermal conductivity, specific heat capacity, and density of the materials, respectively. These data at 293.15 K was cited from COMSOL Multiphysics database.

Materials	Air	SiO_2	PMMA	ZrO_2	TiO_2
κ [W/(m·K)]	0.026	1.367	0.190	1.938	8.687
C_p [J/(kg·K)]	1015.117	703.941	1420	452.863	495.469
ρ [kg/m^3]	1.204	2220.007	1190	6100.001	4249.821

Table 2: Absorptance at $\lambda = 325$ nm used in the simulation for the ZrO_2 and TiO_2 nanoparticles embedded in PMMA containing $Eu(hfa)_3(TPPO)_2$. The extinction values experimentally obtained using the laser light were used as absorptance values for simplicity.

	ZrO_2 in emitter layer	TiO_2 in emitter layer
Absorptance	0.069	0.44

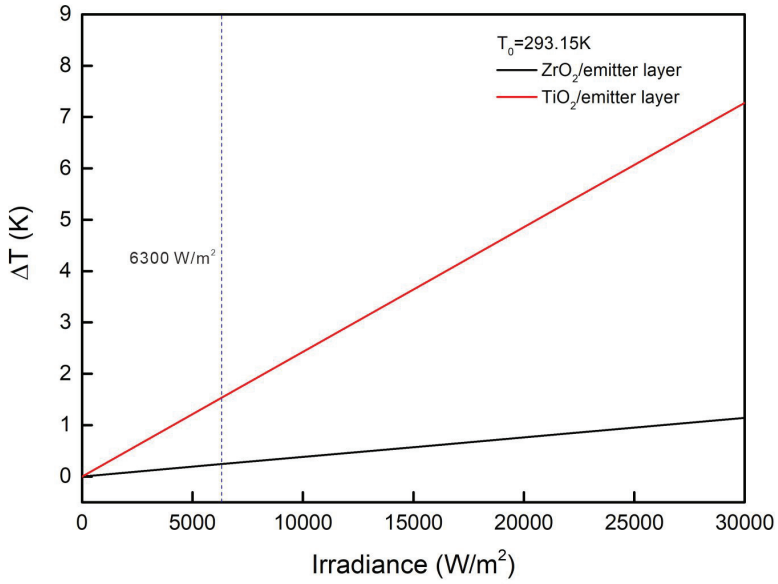

Figure S 11: Simulated increase of temperature (ΔT) at the focus spot as a function of irradiance. The black and red lines represent the ZrO_2 and TiO_2 nanoparticles embedded in PMMA containing $Eu(hfa)_3(TPPO)_2$. The vertical dotted line denotes the experimental value of irradiance.

References

(1) Murai, S.; Verschuuren, M. A.; Lozano, G.; Pirruccio, G.; Rodriguez, S. R. K.; Rivas, J. G. Hybrid plasmonic-photonic modes in diffractive arrays of nanoparticles coupled to light-emitting optical waveguides. *Opt. Express* **2013**, *21*, 4250–4262.

(2) Murai, S.; Gabriel W. Castellanos, G. W.; Raziman, T.; Curto, A. G.; Gómez Rivas, J. Enhanced light emission by magnetic and electric resonances in dielectric metasurfaces. *Adv. Opt. Mater.* **2020**, *8*, 1902024.

(3) Rodriguez, S. R. K.; Murai, S.; Verschuuren, M. A.; Rivas, J. G. Light-Emitting Waveguide-Plasmon Polaritons. *Phys. Rev. Lett.* **2012**, *109*, 166803.